Chronic hyperactivation of midbrain dopamine neurons causes preferential dopamine neuron degeneration

Katerina Rademacher[1,2,3*], Zak Doric[1,2*], Dominik Haddad[1*], Aphroditi Mamaligas[1], Szu-Chi Liao[1,3,4,5], Rose B. Creed[3,6], Kohei Kano[1,3], Zac Chatterton[3,7], Yuhong Fu[3,7], Joseph H. Garcia[1,8], Victoria Vance[1,3,9*], Yoshitaka Sei[1,3], Anatol Kreitzer[1,2,10], Glenda M Halliday[3,7], Alexandra B. Nelson[2,3,6], Elyssa B. Margolis[2,6], Ken Nakamura[1,2,3,6,11]
*equal contribution

[1]Gladstone Institute for Neurological Disease, Gladstone Institutes, San Francisco, CA
[2]Graduate Program in Neuroscience, University of California San Francisco, San Francisco , CA
[3]Aligning Science Across Parkinson's (ASAP) Collaborative Research Network, Chevy Chase, MD
[4]Department of Nutritional Sciences & Toxicology, University of California Berkeley, Berkeley, CA
[5]Endocrinology Graduate Program, University of California Berkeley, Berkeley, CA
[6]UCSF Weill Institute for Neurosciences, Department of Neurology, University of California, San Francisco, CA
[7]Brain and Mind Centre, Faculty of Medicine and Health, School of Medical Sciences, University of Sydney, Sydney, Australia
[8]School of Medicine, University of California, San Francisco, California, USA
[9]College of Science, Northeastern University, Boston, MA
[10]UCSF Department of Physiology, University of California San Francisco, CA
[11]Graduate Program in Biomedical Sciences, University of California San Francisco, San Francisco

*Corresponding author. Tel: (415) 734-2550; Fax: (415) 355-0824; E-mail: ken.nakamura@gladstone.ucsf.edu

Address correspondence to:
Ken Nakamura
Gladstone Institute of Neurological Disease,
San Francisco, CA, 94158
1650 Owens Street
San Francisco, CA 94158
(415) 734-2550 telephone
(415) 355-0824 fax
ken.nakamura@gladstone.ucsf.edu

Abstract

Parkinson's disease (PD) is characterized by the death of substantia nigra (SNc) dopamine (DA) neurons, but the pathophysiological mechanisms that precede and drive their death remain unknown. The activity of DA neurons is likely altered in PD, but we understand little about if or how chronic changes in activity may contribute to degeneration. To address this question, we developed a chemogenetic (DREADD) mouse model to chronically increase DA neuron activity, and confirmed this increase using *ex vivo* electrophysiology. Chronic hyperactivation of DA neurons resulted in prolonged increases in locomotor activity during the light cycle and decreases during the dark cycle, consistent with chronic changes in DA release and circadian disturbances. We also observed early, preferential degeneration of SNc projections, recapitulating the PD hallmarks of selective vulnerability of SNc axons and the comparative resilience of ventral tegmental area axons. This was followed by eventual loss of midbrain DA neurons. Continuous DREADD activation resulted in a sustained increase in baseline calcium levels, supporting an important role for increased calcium in the neurodegeneration process. Finally, spatial transcriptomics from DREADD mice examining midbrain DA neurons and striatal targets, and cross-validation with human patient samples, provided insights into potential mechanisms of hyperactivity-induced toxicity and PD. Our results thus reveal the preferential vulnerability of SNc DA neurons to increased neural activity, and support a potential role for increased neural activity in driving degeneration in PD.

Introduction

In Parkinson's disease (PD), the loss of substantia nigra pars compacta (SNc) dopamine (DA) neurons leads to severe disruption of circuit dynamics in the basal ganglia. Compensation for dopamine loss involves changes in the activity of both surviving SNc neurons, and of other downstream neurons in the circuit. Indeed, following partial lesions of the nigrostriatal pathway in rats, surviving SNc DA neurons are hyperactive (*1*), release additional dopamine (*2-5*), and have reduced dopamine reuptake (*2*). Massive loss of DA neurons (*1, 6, 7*), complete loss of mitochondrial complex I activity (*8*), and loss of the mitochondrial PD protein *PINK1* (*9*) can also result in increased burst firing (*10, 11*). Therefore, DA neurons are predisposed to altered activity in the setting of extensive loss or stress, which may be related to changes at the circuit level. For instance, evidence from primate models suggests that the subthalamic nucleus, which sends a glutamatergic projection to the SNc, is hyperactive in PD (*12*). While system-level changes may be compensatory and partially restore dopamine levels and overall motor function, they may also have adverse consequences. Moreover, critical PD disease proteins including α-synuclein, LRRK2, PINK1, and Parkin can influence the level of neural activity (*13-18*), further supporting the idea that changes in neural activity may also contribute to disease pathophysiology.

Healthy SNc dopamine neurons are believed to have immense energetic requirements due to their pacemaking activity, active Ca^{2+} pumping, unmyelinated or poorly myelinated fibers (*19, 20*) and large axonal arbors (*21*). This large energetic requirement likely accounts for their intrinsic vulnerability to mitochondrial insults, including complex I disruption (*8, 22, 23*) and impairments in mitochondrial dynamics (*24*) and turnover (*25*). It is estimated that about half of the oxygen consumed by mitochondria in SNc DA neurons is devoted to supporting neuronal firing and transmitter release (*26*). Thus, combined with disease-related stress, the metabolic impact of even mild hyperactivity may trigger or accelerate degeneration in SNc DA neurons. In support of this hypothesis, inhibiting the excitatory input from the STN protects SNc DA neurons from 6-OHDA and MPTP toxicity (*27, 28*).

However, empirical evidence linking chronic changes in neural activity to the degeneration of SNc DA neurons in PD is lacking. Recordings from putative SNc neurons in PD patients displayed twofold higher burst firing when compared to recordings from healthy rodents and nonhuman primates despite similar mean firing rates, though this data is difficult to interpret without human controls (*10, 29*). To understand if chronic hyperactivation of DA neurons is sufficient to cause neurodegeneration, we developed a chemogenetic mouse model. Our results indicate that chronically increasing neural activity in midbrain DA neurons results in alteration of circadian locomotion patterns, and prolonged activation leads to selective degeneration of SNc axons and eventual death of midbrain DA neurons. These changes were accompanied by altered intracellular calcium dynamics and transcriptomic changes consistent with calcium dysregulation, supporting a role for increased neural activity in driving neurodegeneration in PD.

Results

To model a chronic increase in DA neuron activity, as may occur in PD, we used a chemogenetic approach. We first expressed the excitatory DREADD hM3Dq specifically in DA neurons using stereotaxic delivery of Cre-dependent hM3Dq AAV to the SNc and VTA of mice expressing Cre under the dopamine transporter (DAT^{IRES}Cre) promoter. Next, we measured the acute behavioral effects of chemogenetic activation of DA neurons. As locomotor output is strongly tied to nigrostriatal dopamine function (*30-32*), we used home cage wheel running as an *in vivo* proxy for changes in dopamine function. Mice were single-housed and locomotion was quantified based on wheel rotation. Two weeks after viral injection, we administered clozapine-n-oxide (CNO) by i.p. injection (0.5mg/kg) and confirmed that mice responded with an acute increase in wheel running as an indicator of successful DREADD expression (Figure S1A). Any non-responders were excluded from the experiment. The resulting hM3Dq-expressing DAT^{IRES}Cre mice were then administered either vehicle (2% sucrose) or CNO (300 mg/L) via drinking water ad libitum for two weeks (Figure 1A). This strategy allowed us to chronically activate SNc and VTA DA neurons.

Previous reports indicate that chemogenetic activation of DA neurons leads to increased locomotion (*33*), but the effects of chronic, long-term activation are unknown. Interestingly, CNO-treated animals showed significant disruptions in circadian activity relative to controls (Figure 1B,C). During the first day of treatment, CNO-treated animals were more active than controls during the dark cycle, and also strongly trended toward more activity during the light cycle. By day 3 of treatment, dark cycle activity markedly decreased in CNO-treated mice, whereas activity during the light cycle remained increased (Figure 1C, Figure S1B). Decreased wheel usage in CNO-treated animals may reflect a consequence of circadian disruption. The prolonged changes in wheel activity indicate that the behavioral effects of chemogenetic activation persist throughout the two-week testing period.

To gain insight into the impact of chronic chemogenetic activation on DA neuron activity, we performed *ex vivo* whole cell recordings in DREADD-expressing SNc neurons in midbrain slices after 7 days of *in vivo* treatment with CNO or vehicle. Chronic *in vivo* DREADD activation induced several changes in somatodendritic properties of SNc neurons including a marked decrease in the magnitude of the hyperpolarization activated non-selective cation current I_h (Figure S1C). It also led to an increase in the spontaneous firing rate (Figure 1D), indicating a chronically increased rate of firing with CNO treatment. The rate of firing was decreased somewhat in controls relative to historical controls from our lab (*24*), possibly reflecting mild chronic stress from the AAV virus. We did not observe a difference in the coefficient of variation of the interspike interval

between treatment groups, thus there was no change in the regularity of pacemaker firing (Figure S1C). *In vivo* CNO led to a more depolarized action potential (AP) peak voltage in spontaneous APs (Figure S1C). *In vivo* treatment did not impact AP threshold voltage or duration (Figure S1C), indicating that AP waveforms were not degraded by *in vivo* CNO treatment.

To measure the direct physiological impact of DREADD activation in SNc neurons, we also acutely bath applied 1 μM CNO to these slices. Interestingly, while SNc neurons from CNO-naïve hM3Dq mice depolarized in response to acute CNO, exposure to chronic *in vivo* CNO eliminated this acute response (Figure 1E). Taken together, these findings indicate that 7d of chronic CNO treatment increased spontaneous firing, but altered hM3Dq function such that acute physiological impacts were no longer apparent. The absence of an acute response may indicate a change in the coupling or availability of the receptors, an adaptation or dysfunction within the neurons, or a homeostatic response to prolonged activation. This may also reflect early stages of toxicity to the CNO-treated DA neurons.

SNc axons are preferentially vulnerable to chronic hM3Dq-activation

To determine if chronic (2-week) chemogenetic activation of DA neurons induces degeneration, we first quantified its effects on axonal integrity in the striatum. Strikingly, compared to vehicle-treated mice, hM3Dq-expressing animals treated with CNO lost ≈40% of their dopaminergic axons in the dorsal striatum, manifest by decreases in both TH immunoreactivity and reporter mCherry immunofluorescence (Figure 2A,B). The same perturbation had a lesser impact on nucleus accumbens and no impact on olfactory tubercle DA afferents.

We also assessed the impact of chronic CNO on DA neuron survival in the midbrain. With stereological quantification we found no difference in neuron number between CNO-treated animals and vehicle-treated controls in the SNc or VTA (Figure 2C). Therefore, at this time point CNO-treated mice exhibit severe axonal degeneration without DA neuron death.

To ensure that the loss of DA terminals was not due to an off-target effect of CNO we chronically administered CNO to animals not injected with AAV-DIO-hM3Dq. These mice did not show a decrease in dopaminergic axons in the caudate putamen (Figure 2D), supporting the conclusion that the axonal degeneration requires hM3Dq activation.

We next assessed the impact of more prolonged chronic activation on degeneration of DA neuron somata. Mice treated with CNO for 4 weeks lost the majority of axons projecting to the caudate putamen (Figure 2E,F), while fibers in the nucleus accumbens and olfactory tubercle were again preferentially spared. Moreover, following 4 weeks of CNO treatment, there was a significant decrease in the overall number of TH+ midbrain (SNc and VTA) DA neurons, assessed by stereology (Figure 2G,H). Although loss of TH reactivity can occur in the absence of neuronal death, there was a similar decrease in the number of mCherry+ DA neurons (labeled by DsRed) in the midbrain, supporting true loss of DA neurons. This suggests that, similar to PD progression in humans (*34*), axonal impairment precedes cell body loss in this model. No preferential loss of SNc versus VTA cell bodies was detected at this time point.

Chronic activation increases baseline population Ca^{2+} levels in midbrain DA neurons

hM3Dq activation may increase neural activity by increasing intracellular Ca^{2+} levels (*35*), and increased neural activity should increase intracellular Ca^{2+}. To determine the impact of chronic hM3Dq activation on intracellular Ca^{2+} concentrations in DA neurons, we bred $DAT^{IRES}Cre$ mice to $GCaMP6f^{fl}$ mice and injected them bilaterally with the Cre-dependent hM3Dq AAV (Figure 3A). The fluorescent signal was used to guide implantation of an optical fiber in the midbrain of animals (Figure 3B,C), with confirmed hM3Dq expression based on increased cage wheel running in response to i.p. CNO (Figure S1A). Mice were administered chronic CNO or vehicle and then

placed in arenas for 10-min fiber photometry recording sessions every 1-3 days over the 2-week treatment period. Mean fluorescence levels served as a proxy for population level intracellular Ca^{2+} concentrations. We observed a small trend for increased fluorescent signal the day after starting CNO that persisted for days 3 through 5 but did not reach significance (Figure 3D-F). Interestingly, this was followed by a second, much larger increase in Ca^{2+} levels between 10-17 days (Figure 3D-F), that occurred in parallel with axon loss (Figure 2A, Figure S1D, Figure S2B). To determine if the increase in neural activity was reversible, we performed two additional recording sessions after removing CNO from the drinking water. Although there was a small trend for decreased fluorescence, this did not reach significance. Together, these data support massive increases in DA neuron intracellular Ca^{2+} over time, which may be due to hM3Dq receptor activation, Ca^{2+} dysregulation, and the onset of degeneration. We also assessed time spent moving and distance traveled during photometry sessions in a subset of animals (Figure S1E). Paralleling the small initial increase in baseline Ca^{2+}, there was a strong trend for CNO to increase activity over time versus controls in both measures of gross locomotion during the first week of treatment (distance traveled $p=0.07$, percent time spent moving $p=0.06$). Interestingly, the increased open field movement in the CNO group decreased back to baseline by day 11 (Figure S1E), just as Ca^{2+} levels begin to climb markedly (Figure 3F), and in parallel to axonal degeneration (Figure 2A, Figure S1D, Figure S2B).

Identifying activation-associated transcriptomic changes with region specificity using spatial transcriptomics

To gain additional insight into the mechanisms of degeneration in this model, we used spatial genomics. We performed Visium spatial transcriptomics on midbrain and striatal sections from DAT^{IRES}Cre mice that were bilaterally injected with AAV-DIO-hM3Dq-mCherry at 3 months and then received either CNO (GqCNO) or vehicle (GqVeh) drinking water for one week prior to harvest. Additional non-injected control mice also received CNO (CNO alone) (Figure 4A). Mice were harvested following one week of CNO treatment in order to quantify transcriptomic changes early in the degeneration process (Figure S1D, Figure S2B), thereby focusing on early gene expression changes prior to degeneration.

We next identified 55 μm diameter barcoded discs (Visium Spatial Gene Expression) overlaying regions enriched for DA neurons within the SN and VTA in the midbrain, and the caudate putamen (CP) (Figure 4B). In the midbrain, selected discs contained at least one entire TH-positive (and mCherry-positive for injected animals) soma, and also expressed at least two of three characteristic DA genes (DAT, vesicular monoamine transporter 2 (VMAT2), or TH) above a pre-set threshold level (Figure 4C). Interestingly, DAT and VMAT2 were significantly decreased in the SN and VTA of GqCNO mice, perhaps indicating a loss of dopaminergic phenotype. Indeed, principal components analyses of the SN and VTA in the midbrain and the CP in the striatum demonstrate that GqCNO midbrain dopaminergic regions are transcriptionally similar to one another and distinct from control groups (Figure 4D). This suggests that chronic DREADD activation induces a robust transcriptomic response in DA neurons that is independent of viral transduction or CNO administration.

We hypothesized that chronic activation of DA neurons likely also leads to specific gene expression changes in striatal target neurons. In the striatum, discs were selected based on expression of *DARPP32* (Figure 4C). Notably, principal components analysis between GqCNO and control groups revealed less separation in the striatum than the midbrain (Figure 4D), perhaps because of the multiple inputs on striatal neurons in addition to dopaminergic axons, although future investigation is required.

We next compared the transcriptomic profiles of discs within each brain region between GqCNO and GqVeh mice, as well as in GqCNO vs CNOAlone mice. Only genes that had significant differential expression between GqCNO and both control groups were assessed for pathway changes (Figure 4E). Consistent with chronic DREADD activation, pathway analyses of GqCNO vs control groups in the SN and VTA showed significant enrichment of GO Biological processes including “chemical synaptic transmission”, “synaptic vesicle exocytosis”, “positive regulation of transporter activity”, and “vesicle transport along microtubule” (Table S1). Also consistent with DREADD activation, GO Molecular Functions in the VTA included “GTP binding” and “syntaxin binding” (Table S1). Interestingly, both CP and SN GO Molecular Functions included “calcium channel regulator activity”, suggesting a larger circuit-level change in Ca^{2+} channel regulation as a result of chronic DREADD activation (Table S1).

Consistent with this, there were a number of differentially expressed genes in the SN and/or VTA that regulate neural transmission, Ca^{2+}, and activity (Figure 4F, Figure S2A, S2C, Figure S3, Figure S4). These included increased expression of S100a6, a Ca^{2+} sensor and modulator (*36*) and Sgk1, a serine/threonine kinase regulated by intracellular Ca^{2+} involved in the regulation of ion channels, membrane transporters, cellular enzymes, and transcription factors (*37*). Interestingly, Sgk1 expression trended up in the CP, supporting circuit-level changes in Ca^{2+} signaling. Increased S100a6 expression has been observed in AD and ALS (*38*), while Sgk1 upregulation has been associated with DA neuron death in rodent toxin models of PD (*39, 40*). Conversely, the expression of calmodulin-2 (Calm2), which mediates control over a large number of enzymes and ion channels as a result of Ca^{2+} binding (*41*), and Trpc6, which is thought to form a non-selective Ca^{2+}-permeant ion channel (*42*) were both decreased. Decreased Trpc6 may be a homeostatic response to chronically high intracellular Ca^{2+}. These changes in Ca^{2+}-regulating genes are consistent with the changes in baseline intracellular Ca^{2+} observed in DA neurons by GCaMP photometry (Figure 3), and may reflect early processes that either cause or contribute to the onset of degeneration, or alternatively compensate to protect against degeneration.

Pathway-level changes in transmission were driven by decreases in several synaptic-vesicle genes, including: synaptotagmin 1, a Ca^{2+} sensor that triggers transmitter release including striatal dopamine release (*43*); Snap25, a t-SNARE that regulates transmitter release (*44*); Ap2a1, a component of the adapter protein complex AP-2 (*45*); and Syngr3, a synaptic vesicle-associated protein that may regulate DAT function (*46*). Interestingly, α-synuclein was also significantly downregulated in the VTA. α-synuclein is enriched in presynaptic terminals, and has been shown to modulate DA release (*47*). Together, these results suggest that chronic DREADD-activation of DA neurons results in significant changes in synaptic transmission which may result in altered Ca^{2+} regulation and DA release.

We also identified differentially expressed genes (DEGs) in the striatum. Upregulated genes included: Mt2, a metallothionein protein that acts as an anti-oxidant to protect against free radicals (*48*); Acsl3, an acyl-CoA synthetase that stimulates fatty acid synthesis (*49*) and could supply energy substrates; and the mitochondrial uncoupling protein Ucp2. Downregulated genes included: Unc13a, which is involved in neurotransmitter release via vesicle maturation and has been implicated in ALS (*50, 51*), and Vgf, a secreted growth factor whose expression is also decreased in PD (*52*).

We also evaluated the SN DEGs (n=59) and additional genes of interest identified within our DREADD mouse model with gene expression changes within human control and early PD subjects (Figure S5A,B). We employed the Nanostring GeoMx assay to assess whole transcriptome changes of dopamine neurons (TH+ masked, see Methods) within the SNc ventral

tier of Controls and Early PD subjects. Of the 59 DEGs, 51 were found within the human dataset, and these genes exhibited broadly congruent directional changes between mouse and human (Chi-square p-value = 0.05). This suggests that similar mechanisms may be at play in the PD midbrain and the DREADD mouse model. To investigate this further, we considered genes that emerged from the mouse dataset involved in Ca2+, transmission, and dopamine, and evaluated them in the early PD samples (Figure S5B, S5C). We found that expression of Syt1, Syngr3, and Calm2 were all decreased in both mouse and human datasets. Similarly, we found that expression of Slc18a2 (VMAT2) and Slc10a4 were also both decreased in the mouse and human data. These findings may suggest common mechanisms of Ca^{2+} dysregulation and altered dopamine metabolism in an early stage of degeneration in our mouse model and in human PD. Additionally, differential gene expression analysis revealed that HSPA4 and EIF3G were downregulated (FDR < 0.02) within the SNc ventral tier DA neurons of early PD subjects compared to controls and in the mouse model (Figure S5A) highlighting other potential common pathogenic mechanisms. Additional investigation is required to determine the functional impact of these genetic changes on dopamine neuron and dopamine neuron subtype function and vulnerability.

Discussion

Here we establish a new model system to chronically activate midbrain dopamine neurons, and show that this chronic activation leads to the preferential and step-wise degeneration of SNc DA neurons, starting with loss of terminals and progressing to neuronal death.

New model to chronically activate DA neurons

Prior studies have activated midbrain DA neurons by both optogenetics and DREADDS to study the impact of DA neuron activity on sleep (*53*) and the spread of pathological α-synuclein (*54*). However, in order to accurately model the impact of neural activity on neurodegeneration, we hypothesized that activity must be chronically increased. Although other studies have used once or twice daily injections of CNO, we delivered CNO in the drinking water to ensure a more continuous, sustained impact on neural activity. We confirmed that chronic hM3Dq activation results in sustained increases in intracellular calcium levels and functional behavioral readouts, suggesting that our model induces long-lasting changes in dopamine neuron activity. Moreover, *ex vivo* electrophysiology demonstrated that the basal level of DA neuron activity does indeed increase with CNO treatment. An important question, however, is whether our model accurately recapitulates how neural activity increases in physiologic or pathologic situations. Increased or decreased rates of DA neuron pacemaking may help to maintain striatal DA as it is depleted in PD, or to protect against energy failure by decreasing energy consumption. Meanwhile, changes in bursting may reflect circuit-level adaptations to PD. Irregular or silenced pacemaking is commonly observed in toxin-based models of PD (*55-59*), while increased induced bursting is observed after massive loss of DA neurons or complete loss of complex I (*1, 6-8*). As such, in future studies it will be important to understand how changes in the pattern of activity (i.e. bursting versus pacing) impact degeneration.

As expected, chronically increasing neural activity increased the movement of mice during the light cycle. However, it was notable that movement as measured by wheel use in the home cage did not increase as robustly as did movement in the open field chamber (Figure S1E), perhaps indicating that the impact on increasing movement is greater in novel environments. This may be a result of the effect of midbrain DA neurons on motivation and exploration (*33, 60*). The later return to control levels of locomotion midway through CNO treatment may indicate the onset of synaptic dysfunction or degeneration. In addition, our electrophysiologic analyses focused on cell body function, but the loss of terminals starting by ≈1 week (Figure S1D, Figure S2B) raises

the possibility that synaptic function might be disrupted even earlier, in parallel to behavioral changes. Meanwhile, chronically increasing activity unexpectedly and robustly decreased movement during the dark cycle (when mice should be most active) within 3-4 days of starting CNO. One possibility is decreased dark cycle movement results from a disruption in sleep, which might occur given the extensive use of running wheels during the light cycle. Indeed, prior studies show that acute inhibition or stimulation of VTA DA neurons by optogenetics or DREADDs suppresses or promotes wakefulness, respectively (*53, 61*). These data support a critical role for VTA DA neurons in maintaining wakefulness, and suggest that increased activity might promote wakefulness in our activity model. Future investigations assessing the impact of chronic SNc versus VTA DA neuron activation on circadian rhythms and sleep are needed to determine if these DA neurons similarly influence sleep in the setting of chronic stimulation, and how potential sleep changes might contribute to the effects of chronically increased neural activity on motor function.

Chronic chemogenetic activation drives degeneration

How does increasing the activity of SNc and VTA DA neurons impact these neurons, as well as their striatal targets? Analysis by spatial transcriptomics near the onset of axonal degeneration reveals a clear decrease in the expression of genes involved in DA synthesis (TH), uptake (DAT) and storage (VMAT2) in the SNc and VTA, perhaps reflecting neuronal stress that precedes degeneration or an attempt to decrease DA release. Decreases in presynaptic transmission-related genes (Syt1, Snap25, Snca, Ap2a1) in midbrain dopamine neurons are consistent with axonal dysfunction and loss that are observed later. Moreover, consistent with the role of hM3Dq DREADDs in increasing cytosolic Ca^{2+} (*35*) on a systems level, we observed a significant change in expression of genes involved in the regulation of calcium channels (Supplemental Table 1), as well as serum and glucocorticoid-inducible kinase 1 (Sgk1), a protein-serine/threonine kinase activated by calcium (*62*), in both the midbrain and striatum. Our photometry analysis also support a central role for Ca^{2+} in activity-induced degeneration, as Ca^{2+} levels in midbrain DA levels rose markedly following 7 days of CNO (Figure 3F), as axonal degeneration progresses (Figure S1D, Figure S2B).

The mechanism of preferential degeneration remains to be determined, but is presumably triggered by increased cytosolic Ca^{2+} levels associated with hM3Dq activation (*35*). SNc DA neurons are believed to be intrinsically vulnerable to increased Ca^{2+} due to their pacemaking activity driven by $CA_V1.3$ channels (*63*), combined with the high energetic requirements of removing Ca^{2+} from neurons and lack of calbindin expression (*64*). Further investigation is required to determine if DREADDs differentially increase Ca^{2+} levels in SNc vs VTA DA neurons, and/or if SNc DA neurons are more vulnerable to the same level of elevation. Further, it remains unknown whether increased Ca^{2+} leads directly to degeneration, for instance by triggering energy failure or increasing ROS, or if it indirectly causes neurodegeneration by triggering potentially toxic downstream processes such as increased cytosolic or extracellular DA release.

If increased DA neuron activity contributes to degeneration in PD, then one might also expect gene expression changes in our model to mirror those seen in PD. Indeed, we found that mouse DEGs exhibited broadly congruent directional changes in the human dataset (Figure S5). This raises the possibility that similar mechanisms of degeneration and adaptation may be at play in both our mouse model and in PD. Interestingly, HSPA4 was significantly downregulated in the mouse and human datasets. Heat shock proteins broadly function to remove misfolded proteins, but the function of HSPA4 in neurons is not well described. However, in rat neural stem cells, HSPA4 is upregulated by selegiline, a type B monoamine oxidase inhibitor used to treat PD, a process that reduces ROS levels and mitochondrial DNA damage following hydrogen peroxide

exposure (*65, 66*). In MPTP-treated mice, deacetylation of HSPA4 is linked to decreased microglial activation and neuroinflammation (*67*). In our activity model, decreased HSPA4 expression might indicate a failure to respond to inflammation, promoting neurodegeneration. Further studies will be required to investigate the role of HSPA4 and inflammation in chronic hyperactivation-induced toxicity.

It is important to note that our transcriptomic analysis has limited cell type resolution due to the size of spatial transcriptomic capture discs, which include other cells in addition to DA neurons. Therefore, important areas of future investigation include higher spatial resolution in the analysis of mouse tissue, and assessment of additional brain areas and cell types in human PD patient tissues.

In some cases, disease proteins or circuit changes may have the converse effect of decreasing activity. As such, it will be important to understand in which contexts activity increases or decreases, and also how decreasing DA activity influences degeneration. Indeed, if activity does promote degeneration, it will also be important to understand if decreasing DA neuron activity is protective, and if activity can be decreased or modulated without compromising motor function. Interestingly, chronic nicotine, which may mediate the protective association of smoking in PD (*68, 69*), inhibits SNc DA neurons through agonism of nicotinic acetylcholine receptors expressed on presynaptic GABAergic terminals (*70*). In addition, a proposed mechanism of action for the beneficial effects of deep brain stimulation (DBS) in PD is the inhibition of the subthalamic nucleus. As such, it will also be important to know how DBS influences DA neuron activity and if it has the potential to influence neurodegeneration. Interestingly, recent clinical trial data raise the possibility that DBS may slow disease progression when administered to early-stage patients (*71*).

In summary, our data show that chronically increasing the activity of DA neurons can produce toxicity. Considering that DA neuron activity may increase to compensate for other dying DA neurons, or in response to certain disease proteins, our data support the hypothesis that increased neural activity contributes to the pathophysiology of at least a subset of PD. Proving this, and determining how this evolves with disease stage, will be important goals for future research.

FIGURE LEGENDS

Figure 1. Chronic hM3Dq activation chronically alters the activity of SNc dopamine neurons.
(A) Graphical illustration summarizing experimental design. Recombinant AAV encoding a conditional allele of the hM3Dq(DREADD)-mCherry was injected bilaterally into the ventral midbrain of 4-5 month-old DAT^{IRES}Cre mice. CNO (300 mg/L) or vehicle (2% sucrose in water) was administered *ad libitum* via drinking water for two weeks and the animals perfused the next day. Changes in locomotion were assessed with running wheels. The two days preceding start of treatment were used as a measure for baseline locomotion.
(B) Representative traces of wheel usage for animals given control vehicle water (top) or CNO water (bottom). Arrows denote start of treatment. Grey background shading indicates dark cycle hours.

(C) Mean wheel usage for selected days during the experiment, segregated by light (left) or dark (right) cycles. n=10 animals/group from 2 independent experiments. *p≤0.05, **p<0.01, ***p<0.001 by two-way ANOVA and Holm-Sidak post hoc test.
(D) Spontaneous firing rate was measured during the first 2 min of whole cell recordings. **p ≤ 0.01, ***p ≤ 0.005 by t-test or permutation (non-parametric) analysis.
(E) Time course of responses to bath application of 1 μM CNO *ex vivo* measured in current clamp in neurons from vehicle-treated mice: 4.9 +/- 2.9 mV (n = 5), in neurons from CNO-treated mice: -0.5 +/- 1.0 mV (n = 9); p = 0.05, t test.

Figure 2. Chronic activation with AAV-hM3Dq-DREADDs is preferentially toxic to nigrostriatal axons.
DAT^{IRES}Cre mice expressing hM3Dq(DREADD)-mCherry **(A-C, E-H)**, or no virus injection **(D)** in DA neurons. Example images of TH **(A,D,E)** and mCherry **(B,F)** immunoreactivity in striatal sections of mice treated for two or four weeks with vehicle **(left)** or CNO **(right)** via drinking water. DA neuron projection areas in dorsal and ventral striatum are indicated with dotted lines. Quantifications for TH (A,D,E) and mCherry (B,F) optical density at 2 and 4 weeks show preferential loss in CPu. n = 8-9 animals/group, 3-5 sections/animal, from two independent experiments. **(C,G,H)** Images of TH and mCherry (4 weeks only) immunoreactivity in midbrain of vehicle **(top)** or CNO **(bottom)** treated mice at 2 or 4 weeks. SN and VTA regions are indicated with dotted lines. (C,G,H) Stereology estimating the number of TH+ or mCherry+ DA neurons. Chronic CNO treatment of hM3Dq(DREADD)-expressing mice shows a significant decrease in both TH and mCherry immunoreactivity and DA neuron number. n = 4-5 (A,C, E-H) or 3 (D) animals/group. Scale bars indicate 100μm in the midbrain and 200μm in the striatum. Error bars indicate mean ± SEM. *p<0.05, **p<0.01, ***p < 0.001 by two-way ANOVA and Holm-Sidak *post hoc* test. SN: substantia nigra, VTA: ventral tegmental area, CPu: caudate putamen, NAc-C: nucleus accumbens core, NAc-Sh: nucleus accumbens shell, OT: olfactory tubercule.

Figure 3. Chronic hM3Dq activation increases baseline calcium in parallel with axonal degeneration.
(A) Transgenic mice expressing Ca^{2+}-reporter GCaMP6 specifically in DA neurons were injected bilaterally with AAV-DIO-hM3Dq-mCherry and implanted with an optical probe for baseline Ca^{2+} measurements during a 14-day chronic chemogenetic activation.
(B) Representative image of photometry probe placement in mouse midbrain to record from dopamine neurons co-expressing hM3Dq-mCherry (magenta) and GCaMP6 (cyan). Scale bar is 200 μm.
(C) Representative high-magnification images of GCaMP6 (cyan), mCherry reporter (magenta) and co-expression. Scale bar is 10 μm.
(D) Representative raw traces of baseline Ca^{2+} fluorescence in mice treated with vehicle vs CNO.
(E) Representative isosbestic corrected traces in mice treated with vehicle vs CNO.
(F) Baseline Ca^{2+} fluorescence levels of DA neurons in mice treated with vehicle or CNO for 14 days (gray shaded area), and following wash. Error bars indicate mean ± SEM. *, p<0.05 by two-way ANOVA, n = 7 mice/group from 2 independent experiments.

Figure 4. Spatial transcriptomics reveals midbrain DA and striatal target DEGs altered by chronic DA neuron hyperactivity
(A) DAT^{IRES}Cre animals that received CNO (CNO only, n=2 mice) or were injected with AAV-hM3Dq-mCherry and received vehicle (GqVeh, n=3 mice) or CNO (GqCNO, n=3 mice) were administered CNO for one week before brains were flash frozen for spatial transcriptomic analysis.

(B) Image of midbrain and striatal sections stained with TH (green), NeuN (purple), and DAPI (blue) shows discs assigned to regions of interest. Inset shows a disc containing two TH+ cell bodies. Scale bars indicate 500µm.
(C) Expression of dopaminergic and striatal genes is confined to expected spatial regions. Expression of genes involved in DA metabolism decrease with chronic CNO. 2-49 discs were compiled per VTA and 1-7 discs were compiled per SN. 357-560 capture areas were compiled per CP. The thalamus was selected as a midbrain control region, while white matter tracts (white) and the lateral septal complex (LSX) were used as striatal controls. *p<0.05, **p<0.01, ***p<0.001 by one-way ANOVA followed by Holm-Sidak *post hoc* test in the SN, VTA, and CP.
(D) Principal components analysis of midbrain regions (left) and the caudate putamen (right) for GqCNO, GqVeh, and CNO only groups.
(E) Hits were used for Enrichr pathway analysis if significant in both GqCNO vs CNO alone and GqCNO vs GqVeh comparisons. Gene rankings for hit analysis were established using fold change score (FCS) and signal-to-noise score (SNS).
(F) Volcano plots comparing GqCNO vs GqVeh in the SN, VTA, and CP. Genes highlighted are also significantly altered when comparing GqCNO vs CNO only.

Figure S1. Full activity traces and additional electrophysiological properties.
(A) Representative running wheel traces of a $DAT^{IRES}Cre$ mouse injected with AAV-hM3Dq(DREADD)-mCherry following i.p. injection of either saline (left) or CNO (right). Dotted line indicates time of injection.
(B) Average running wheel rotations per minute over 12-hour light (top) and dark (bottom) cycles for two independent cohorts of $DAT^{IRES}Cre$ mice injected with AAV-hM3Dq(DREADD)-mCherry. CNO (300 mg/L) or vehicle (2% sucrose in water) was administered *ad libitum* via drinking water for two weeks and the animals perfused the next day. Some data was lost from days 2-6 and 13-14 due to technical issues during Cohort 2. Open circles in light cycle denote incomplete datasets (3hrs). n=5 animals/group.
(C) SNc DA neurons expressing the DREADD and activated chronically *in vivo* showed alterations in CNO responses and overall physiology. I_h magnitude was measured in whole cell voltage clamp configuration, $V_{holding}$ = -60 stepping to -120 mV in neurons from vehicle-treated cells vs CNO-treated cells. Firing regularity and input resistance were measured during the first 2 min of whole cell recordings. Spontaneous AP waveforms were compared across groups for threshold membrane potential, peak membrane potential, and duration. ** $p \leq 0.01$, *** $p \leq 0.005$ by t-test or permutation (non-parametric) analysis.
(D) Example images of TH immunoreactivity in striatal sections of mice treated for one week with vehicle **(left)** or CNO **(right)** via drinking water. DA neuron projection areas in dorsal and ventral striatum are indicated with dotted lines. Quantification for TH optical density shows a trend for preferential loss in CPu. n = 5 animals/group, 3-5 sections/animal. Scale bar indicates 200µm. Error bars indicate mean ± SEM. Analyzed by two-way ANOVA and Holm-Sidak *post hoc* test. CPu: caudate putamen, NAc-C: nucleus accumbens core, NAc-Sh: nucleus accumbens shell, OT: olfactory tubercule.
(E) Distance traveled (left) and percent time spent moving (right) during photometry sessions in mice treated with vehicle or CNO for 14 days (gray shaded area) and following wash. Error bars indicate mean ± SEM. N = 3-4 mice/group.

Figure S2. Additional spatial transcriptomic data following chronic hyperactivation.
(A) Volcano plots comparing GqCNO vs CNO Only in the SN, VTA, and CP.

(B) Anti-TH immunofluorescence of striatal sections processed for spatial transcriptomics demonstrate loss of TH+ fibers in GqCNO sections after one week of chronic hyperactivation (white arrows). Scale bars indicate 1mm.
(C) Bar graphs of individual midbrain and striatal genes of interest. *p<0.05, **p<0.01, ***p<0.001 by one-way ANOVA followed by Holm-Sidak *post hoc* test.

Figure S3. Top differentially expressed genes in the mouse SN and VTA.
Heatmaps of the top differentially expressed SN and VTA genes, expressed as the $\log_2$ fold score.

Figure S4. Top differentially expressed genes in the mouse CP.
Heatmaps of the top differentially expressed CP genes, expressed as the $\log_2$ fold score.

Figure S5. Assessment of mouse DEGs in human PD and control SNc samples.
Heatmap of normalized gene expression (per ROI) values from GeoMx spatial transcriptomic analysis of human SNpc ventral tier dopamine neurons (TH+) within **(A)** 51 DEGs and **(B)** additional genes of interest identified within the mouse model. N = 10 control and 8 early PD samples. 'Limma voom' methodology was used to assess differential gene expression between control and PD samples. PMD, post-mortem delay; DV200, RNA integrity number equivalent.

Supplementary Table S1. Pathway analyses for the VTA, SN, and CP following chronic hyperactivation.
Gene Ontology Molecular Function and Biological Process terms for differentially expressed genes in the VTA, SN, and CP generated with the Enrichr webtool.

Supplementary Table S2. Demography of the human post-mortem cohort assayed by GeoMx.
Values are presented as median (IQR). The comparison of Age at death, Post-mortem delay and DV200 between groups was made using the Welch Two Sample t-test. The comparison of gender between groups was made using chi-square test. * P < 0.05, ** P < 0.001.

Methods

Experimental model and subject details

Mice
Mice were group-housed in a colony maintained with a standard 12-hour light/dark cycle and given food and water ad libitum. All mice received food on the cage floor. All animal experimental procedures were conducted in accordance with the Guide for the Care and Use of Laboratory Animals, as adopted by the National Institutes of Health, and with approval from the University of California, San Francisco Institutional Animal Care and Use Committee. All mice were housed in a state-of-the-art barrier facility managed by the UCSF Laboratory Animal Resource Center (LARC). Animal care and use in this research are covered under the UCSF "Assurance of Compliance with PHS Policy on Humane Care and Use of Laboratory Animals by Awardee Institutions" number A3400-01. Experiments were performed on age-matched mice. All mouse lines were maintained on a C57Bl/6 background (The Jackson Laboratory; RRID:IMSR_JAX:000664). DAT^{IRES}Cre mice (*72*) were obtained from the Jackson laboratory.

Methods

Chemogenetics

A detailed protocol for mouse stereotaxic surgery can be found at https://dx.doi.org/10.17504/protocols.io.b9kxr4xn. DAT^{IRES}Cre mice (RRID:IMSR_JAX:006660) were injected bilaterally with rAAV8-hSyn-DIO-hM3Dq-mCherry (UNC Vector Core, AddGene, RRID: Addgene_50459) into the midbrain (-3.0 mm anterior-posterior, ±1.2 mm medial-lateral, -4.3 mm dorsal-ventral) using a stereotaxic frame (Kopf) and a microliter syringe (Hamilton).

A detailed protocol for monitoring mouse activity can be found at dx.doi.org/10.17504/protocols.io.3byl4qqe8vo5/v1. Two weeks following surgery, animals were single-housed and habituated to wireless running wheels (MedAssociates ENV-047, RRID: SCR_024879) connected to a hub (MedAssociates DIG-807, RRID: SCR_024880,) for locomotion recordings and water bottles (Amazon) for drinking. A detailed protocol for validating responsiveness of DREADD-injected DAT^{IRES}Cre mice to CNO can be found at dx.doi.org/10.17504/protocols.io.6qpvr3yrpvmk/v1.

A detailed protocol for preparing and administering CNO via drinking water can be found at dx.doi.org/10.17504/protocols.io.n2bvj33oblk5/v1. CNO (NIMH, Tocris 4936) was administered ad libitum in 2% sucrose water at 300mg/L. CNO and vehicle waters were made fresh weekly and stored at 4˚C protected from light.

Ex Vivo Recording

A detailed protocol for ex vivo electrophysiology can be found at dx.doi.org/10.17504/protocols.io.261gedqn7v47/v1. DAT^{IRES}Cre mice injected bilaterally with rAAV8-hSyn-DIO-hM3Dq-mCherry and chronically treated with vehicle or CNO for one week were provided to the electrophysiologist blind to in vivo treatment. Mice were deeply anesthetized with isoflurane, decapitated with a rodent guillotine, and the brains were removed. Horizontal brain slices (150 um thick) containing the SNc were prepared using a Vibratome (Campden Instruments,7000smz-2). Slices were cut in ice cold aCSF solution containing (in mM): 119 NaCl, 2.5 KCl, 1.3 $MgSO_4$, 1.0 NaH_2PO_4, 2.5 $CaCl_2$, 26.2 $NaHCO_3$, and 11 glucose saturated with 95% O_2–5% CO_2 and allowed to recover at 33°C in aCSF for at least 1 hr.

Slices were visualized under an *Axio Examiner A1* equipped with Dodt and IR optics, using a Zeiss Axiocam 506 mono and Neurolucida 2023 (MBF Biosciences) software. Neurons were identified as DREADD-expressing prior to patching with fluorescent imaging of mCherry expressed concurrently with DREADDs. Whole-cell patch-clamp recordings were made at 33°C using 3– 5 MOhm pipettes containing (in mM): 123 K-gluconate, 10 HEPES, 0.2 EGTA, 8 NaCl, 2 MgATP, and 0.3 Na_3GTP, pH 7.2, osmolarity adjusted to 275. Biocytin (0.1%) was also included in the internal solution to identify neurons after recordings where desired.

Recordings were made using Sutter IPA and SutterPatch v2.3.1 software (Sutter Instruments), filtered at 5 kHz and collected at 10 kHz. Liquid junction potentials were not corrected. I_h was recorded by voltage clamping cells at -60 mV and stepping to -40, -50, -70, -80, -90, -100, -110, and -120 mV. Cells were recorded in current-clamp mode (I= 0 pA) for measuring spontaneous firing rates and CNO responsivity. For CNO testing, spontaneous firing rate or resting membrane potential were monitored until a stable baseline was observed for at least 5 min. Then perfusion solution was switched 1 uM CNO for 5 min.

When recordings were completed, slices were drop fixed in 4% formaldehyde in PBS for at least 2 hr.

For quantifications, spontaneous firing rate was measured as the mean firing rate during the first 120 sec of whole cell recording. Once every 10 sec a brief hyperpolarizing pulse was applied, and the input resistance of the neuron was quantified from this test, averaged across the measurements made during the first 2 min of recording. AP waveform measurements were made from averages across at least 8 APs from this recording interval. I_h magnitude was quantified as the difference between the initial steady state response to the -120 mV step and the asymptote of the slow current sag.

Statistical analyses were completed in R (4.2.3), first testing whether data met the criteria for parametric statistical evaluation. Those datasets that met criteria were compared by unpaired Student's t-test. Those that did not meet these criteria were compared by permutation test. Code for the electrophysiology analysis can be found on GitHub at https://github.com/eb-margolis-neuroscience-lab/R-general-Margolislab/blob/main/permtestsEBM.R.

All salts and reagents were purchased from Sigma except CNO (Tocris).

Ex Vivo Data Analysis

Results are presented as mean ± S.E.M or with kernel density estimations. All but 1 neuron recorded in current clamp was quiescent during CNO testing. This neuron both depolarized and increased firing rate in response to CNO and therefore was included in the time course average figure. For all data parametric assumptions were tested to choose between t-test (parametric) or permutation (non-parametric) analysis.

Fiber photometry

A detailed protocol for collecting fiber photometry data can be found at dx.doi.org/10.17504/protocols.io.bp2l6xwxzlqe/v1. 3-month-old Ai148 mice (RRID:IMSR_JAX:030328) bred with DAT^{IRES}Cre were injected with rAAV8-hSyn-DIO-hM3Dq-mCherry as described above. After allowing 3 weeks for expression of the hM3Dq construct, locomotion was tested using IP injection of CNO to determine robust hM3Dq expression. Mice that exhibited increased locomotion following CNO injection were then implanted with optical fibers (400 µM, 0.48 NA). Mice were administered vehicle or CNO water for 14 days.

In vivo calcium data was acquired using a custom-built photometry system. An RZ5P fiber photometry processor (TDT, RRID: SCR_024878) and Synapse software (TDT, RRID: SCR_006307) were used to control LED output and acquire the photometry signal. Using this system, two LEDs were used to control GCaMP and isosbestic excitation (470 nm and 405 nm, respectively, Thorlabs). LEDs were sinusoidally modulated at 211 Hz (470 nm) and 531 Hz (405 nm) and entered a four-port fluorescence mini cube (Doric Lenses). The combined output was coupled to a fiber-optic patch cord (400 µm, 0.48 NA, Thorlabs), which then mated to the fiberoptic cannula in the mouse brain. The emitted light was collected onto a visible femtowatt photoreceiver module (AC low, Newport) and sampled at 60 Hz. Photometry data was then extracted via proprietary TDT software using MATLAB (MathWorks, RRID: SCR_001622).

Open Field Behavior

A detailed protocol for open field analysis can be found at dx.doi.org/10.17504/protocols.io.36wgq33rklk5/v1. Spontaneous locomotor activity was assessed while simultaneously recording fiber photometry data. Videos acquired during photometry sessions were analyzed using Ethovision software (Noldus, RRID: SCR_000441) to calculate total distance traveled and percent of time spent moving.

Immunohistochemistry

Animals were anesthetized with 2,2,2-tribromoethanol and perfused with PBS followed by 4% paraformaldehyde (PFA) in PBS. Intact brains were removed, post-fixed in 4% PFA overnight at 4ºC and cryoprotected in 30% sucrose. 40-µm-thick coronal sections were cut on a sliding microtome (Leica) and stored in cryoprotectant (30% Ethylene Glycol (Sigma), 30% Glycerol (Fisher scientific) in PBS).

A detailed protocol for immunofluorescence can be found at dx.doi.org/10.17504/protocols.io.kxygx38owg8j/v1. Brain sections were rinsed with PBS followed by 0.2% Triton X-100 in PBS. The sections were then transferred to a blocking solution containing 4% fetal bovine serum (JR Scientific) and 0.2% Triton X-100 in PBS for 1 hour. Following overnight incubation in primary antibody, sections were rinsed in 0.2% Triton X-100 in PBS and incubated for 2 hours with a suitable secondary antibody. Sections were rinsed again in 0.2% Triton X-100 before mounting with antifade mounting medium (Vector Laboratories H1400, H1500).

A detailed protocol for peroxidase staining can be found at dx.doi.org/10.17504/protocols.io.n92ldm127l5b/v1. Sections were quenched with 3% H_2O_2 and 10% methanol in PBS and blocked in 10% fetal bovine calf serum, 3% BSA, 1% glycine, and 0.03% sodium azide in PBS with 0.5% Triton X-100. They were incubated with primary antibody followed by biotinylated secondary and subsequently streptavidin-conjugated horseradish peroxidase (HRP) (1:500; Vectastain ABC kit, Vector Laboratories). Immunostaining was visualized with hydrogen peroxide and 1 3,3′-diaminobenzidine (DAB, Sigma).

The following primary antibodies were used: rabbit anti-DsRed (1:1000; Takara, RRID: AB_3083500), rabbit anti-tyrosine hydroxylase (1:1000; AB152, Millipore, RRID: AB_390204), mouse anti-NeuN (Millipore MAB 377, RRID: AB_2298772), and chicken anti-mCherry (Abcam ab205402, RRID: AB_2722769). Secondary antibodies Alexafluor goat anti-mouse 647 (Thermo Fisher Scientific Cat# A-21235, RRID:AB_2535804), anti-rabbit 488 (Thermo Fisher Scientific Cat# A11034, RRID:AB_2576217), anti-rabbit 594 (Thermo Fisher Scientific Cat# A11037, RRID:AB_2534095), or anti-chicken 594 (Thermo Fisher Scientific Cat# A-11042, RRID:AB_2534099) IgG were used (1:500). A biotinylated goat anti-rabbit IgG (1:300, Vector Laboratories, BA-1000, RRID:AB_2313606) was used for peroxidase staining.

Stained samples were visualized using an automated fluorescence microscope (Keyence BZ7000) and a laser-scanning confocal microscope (Zeiss LSM880).

Stereology

Total numbers of TH- and mCherry-positive neurons were quantified blinded to groups. Region selection of SN and VTA was done under 5× magnification following the definition by Fu and colleagues (*73*). Imaging was done under 63× magnification by a Zeiss Imager microscope (Carl Zeiss Axio Imager A1) equipped with an XYZ computer-controlled motorized stage and an EOS rebel T5i Digital Camera (Canon), and counting was done using MBF Bioscience's Stereo

Investigator (RRID: SCR_024705). Counting frame size was 60 × 60 μm and systematic random sampling (SRS) grid was 130 × 130 μm, with a section interval of 6.

Optical density analysis

A detailed protocol for optical density analysis can be found at dx.doi.org/10.17504/protocols.io.81wgbxo2nlpk/v1. Images of DAB-stained striatal sections were taken with an automated light microscope (Keyence) by a blinded experimenter. ImageJ (RRID: SCR_002285) was calibrated for optical density and subsequently used to draw ROIs around striatal areas and to measure mean optical density. The Allen Brain Atlas was used as a reference brain atlas (Allen Mouse Brain Atlas, mouse.brain-map.org and atlas.brain-map.org). Optical density values were background subtracted using an adjacent brain region with low TH expression levels, the piriform cortex.

Spatial Genomics

Mouse Spatial Gene Expression

Spatial transcriptomics were acquired with Visium spatial gene expression kits (10X Genomics). Sample preparation, sample imaging, and library generation were completed in accordance with 10X Spatial Gene Expression protocols and as previously published (*74*). Briefly, fresh brain tissue was flash frozen in an isopentane bath cooled to -80˚C using dry ice. The brain tissue was then embedded in Optimal Cutting Temperature (OCT) compound (Tissue-Tek 62550-12). A cryostat was used to obtain a 10 μm thin section from the midbrain that was then mounted onto a 10X spatial gene expression slide. Sections were stained with TH, NeuN, and DsRed to visualize mCherry (striatal sections only), and Hoechst 33342 before imaging on a Leica Aperio Versa slide scanner. The cDNA libraries were generated at the Gladstone Genomics Core. Libraries were sequenced at the UCSF Center for Advanced Technology on an Illumina NovaSeq 600 on an SP flow cell. Alignment of the sequencing data with spatial data from the Visium slide was completed with the 10X Space Ranger software (10x Genomics, RRID: SCR_023571). The 10X Loupe Browser software (RRID: SCR_018555) was then used to identify six anatomical regions of interest: (1) SN, (2) VTA, and (3) thalamus in the midbrain, and (4) CP, (5) LSX, and (6) white matter tracts in the striatum. RNA capture areas corresponding to each anatomical region were selected for analysis based on their spatial proximity to the anatomical regions and on the expression of known genetic markers. SN and VTA genetic markers included TH, DAT, and VMAT2; thalamus markers included Prkcd, Ptpn3, and Synpo2; CP was identified with DARPP32; the LSX was identified with PRKCD; white matter was identified with MBP. Demarcation of SN and VTA was done according to Fu and colleagues (*73*). Capture areas that expressed high levels of astrocyte markers (Gfap, Aldh1l1) and microglia markers (Aif1, P2ry12) were excluded. SN and VTA capture areas also had to contain at least one complete DA neuron soma. Roughly 5-10 neuronal cell bodies fit into a single capture area for SN and VTA with 2-49 capture areas per VTA, 1-7 capture areas per SN, 0-39 capture areas per thalamus, 357-560 capture areas per CP, 6-93 capture areas per LSX, and 21-72 capture areas per white matter tracts. Gene expression levels were exported to GraphPad Prism and Microsoft Excel (Microsoft, RRID: SCR_016137). Gene rankings for hit analysis were established using the fold change score (FCS) and signal-to-noise score (SNS). Equations for these scores are given as:

$$SNS = \frac{\mu_{KO} - \mu_{WT}}{\sigma_{KO} + \sigma_{WT}} \times (-Log_{10}P)$$

$$FCS = Log_2\left(\frac{\mu_{KO}}{\mu_{WT}}\right) \times (-Log_{10}P)$$

where μ is the average gene expression, σ is the standard deviation, and P is the p-value derived from a t-test. Genes with a p-value < 0.05 were highlighted as differentially expressed genes of interest. The expression levels for these genes of interest were probed in SN, VTA, and the thalamus to identify a subset of genes with DA region-specific changes. Pathway analysis was done on all hits that appeared in both scoring metrics using the Enrichr webtool (RRID: SCR_001575) (*75-77*). Code for spatial transcriptomics analysis can be found on GitHub at https://github.com/yoshitakasei/NakamuraVisiumR-Analysis.

Principal Components Analysis

The R function prcomp was used for principal component analysis, with the median normalized gene expression level of each gene as the input. Only genes that were expressed in all regions (for SN and VTA) and whose expression was >0 were included.

Human Spatial Gene Expression

Cohort materials: Formalin-fixed paraffin-embedded (FFPE) midbrain sections were collected from individuals with pathologically verified early-stage Parkinson's Disease (ePD) (n=10) and individuals without any neurological or neuropathological conditions (n=10) through the New South Wales (NSW) Brain Banks, as detailed in Supplementary Table 2. The research protocol received ethical clearance from the University of Sydney Human Research Ethics Committee (approval number 2021/845). All PD subjects exhibited a positive response to levodopa and met the UK Brain Bank Clinical Criteria for PD diagnosis (*78*) without any other neurodegenerative disorders. Control subjects demonstrated no signs of Lewy body pathology, and ePD subjects had Braak stage IV Lewy body pathology, in accordance with established criteria (*79, 80*).

Sequencing and data processing: FFPE sections were stained using TH antibody (BioLegend, cat# 818008, 1:50 RRID: AB_2801155) and processed using the Nanostring GeoMx® Digital Spatial Profiler (RRID: SCR_021660), as per manufacturer instructions, to obtain TH+ masked transcripts. Sequencing libraries for the whole transcriptome were constructed using the Human Whole Transcriptome Atlas (GeoMx Hu WTA) following manufacturer instructions. Technical replicates were consolidated using the Linux 'cat' command, and alignment and feature counting were performed using the GeoMx NGS analysis pipeline (version 2.0.21) executed on the Illumina BaseSpace platform (Illumina, RRID: SCR_011881). Quality control was implemented using R statistical programming language with the cutoffs; minSegmentReads: 1000, percentTrimmed: 80%, percentStitched: 80%, percentAligned: 75%, percentSaturation: 50%, minNegativeCount: 1, maxNTCCount: 10,000, minNuclei: 20, minArea: 1000. The minimum gene detection rate across all samples was set at 1%. The minimum gene detection rate per sample was set to 1%. Recently, Van Hijfte and colleagues reviewed the recommended Nanostring GeoMx Q3 normalization technique (*81*), observing that Q3 normalization failed to correct for large differences in the signal (gene expression) to noise (neg probes) observed between samples and recommended quantile normalization. We performed preliminary experiments of 5 normalization techniques; Q3 normalization, background normalization, quantile normalization, SCTransform and normalizing for total library size. We observed that quantile normalization displayed the lowest absolute MA plot correlation and least significance following Kolmogorov Smirnov test. Hence, quantile normalization was implemented, and batches (slides) were corrected using Harmony (*82*), DEGs identified by spatial transcriptomic analysis of mouse model were evaluated between control and ePD TH+ masked Regions of Interest (ROIs) from the SNc ventral tier. The

congruence between directional changes of mouse and human was quantified using a chi-square test. To assess differential gene expression between control (CTR) and Parkinson's disease (PD) samples, we employed the 'limma voom' methodology, incorporating covariates diagnosis, age, post-mortem delay (PMD), RNA integrity number equivalent (DV200), sex, DSP processing plate, and brain bank ID (*83*). This analysis was conducted using the R statistical software environment with all scripts are available at https://github.com/zchatt/ASAP-SpatialTranscriptomics/tree/Rademacher_2024 and processed and raw datasets are available at 10.5281/zenodo.10499186.

Quantification and Statistical Analysis

All statistical analyses including the n, what n represents, description of error bars, statistical tests used and level of significance are found in the figure legends. Two-way repeated-measures ANOVA followed by Holm-Sidak multiple comparisons was used for comparing vehicle vs CNO groups. One-way ANOVA followed by Holm-Sidak multiple comparisons was used for comparing multiple groups in mouse spatial transcriptomic data. T-test or permutation (non-parametric) analysis was used for ex vivo electrophysiology data. Mouse differentially expressed genes were ranked according to the defined SNS and FCS metrics. Congruence between directional changes of mouse and human was quantified using a chi-square test. 'Limma voom' methodology was used to assess differential gene expression between control and PD samples, incorporating covariates (see Human Spatial Gen Expression). All analyses were performed using GraphPad Prism version 9 (RRID: SCR_002798), Microsoft Excel, and R version 4.2.2 (RRID: SCR_000432).

Data, Materials, and Software Availability

Datasets are available at https://doi.org/10.5281/zenodo.10499027. All other data are included in the manuscript and/or supporting information.

Conflict of Interest Statement

The authors declare no competing interests. Anatol Kreitzer's current role is Chief Discovery Officer at Maplight Therapeutics.

Acknowledgements

We acknowledge Haru Yamamoto for assistance preparing the manuscript, and Kathryn Claiborn for helping edit the manuscript and Erica Delin for administrative assistance. We thank Saheli Singh for assistance with mouse spatial transcriptomics analysis, Robert Edwards, Zayd Khaliq, Talia Lerner and Christopher Ford from "Team Edwards" for feedback on experiments, and Yutau Liu for technical assistance.

This research was funded in whole or in part by Aligning Science Across Parkinson's (ASAP-020529) through the Michael J. Fox Foundation for Parkinson's Research (MJFF). For the purpose of open access, the author has applied a CC BY public copyright license to all Author Accepted Manuscripts arising from this submission. This work was also supported NIH (RO1NS091902, KN), the Joan and David Traitel Family Trust and Betty Brown's Family, a Burroughs-Wellcome Fund Award (KN), and the Gladstone Institutes. This work was also supported by the Hillblom Foundation (ZD) and a Berkelhammer Award for Excellence in Neuroscience (ZD).

References

1. J. R. G. Hollerman, A. A., The effects of dopamine-depleting brain lesions on the electrophysiological activity of rat substantia nigra dopamine neurons. *Brain Research* **533**, 203-212 (1990).
2. M. J. Zigmond, A. L. Acheson, M. K. Stachowiak, E. M. Stricker, Neurochemical compensation after nigrostriatal bundle injury in an animal model of preclinical parkinsonism. *Arch Neurol* **41**, 856-861 (1984).
3. Y. Agid, F. Javoy, J. Glowinski, Hyperactivity of remaining dopaminergic neurones after partial destruction of the nigro-striatal dopaminergic system in the rat. *Nat New Biol* **245**, 150-151 (1973).
4. F. Hefti, E. Melamed, R. J. Wurtman, Partial lesions of the dopaminergic nigrostriatal system in rat brain: biochemical characterization. *Brain Res* **195**, 123-137 (1980).
5. W. Q. Zhang *et al.*, Increased dopamine release from striata of rats after unilateral nigrostriatal bundle damage. *Brain Res* **461**, 335-342 (1988).
6. L. Chen *et al.*, Chronic, systemic treatment with a metabotropic glutamate receptor 5 antagonist in 6-hydroxydopamine partially lesioned rats reverses abnormal firing of dopaminergic neurons. *Brain Res* **1286**, 192-200 (2009).
7. M. K. K. J. R. W. S. Stachowiak, E. M.; Zigmond, M. J., Increased dopamine efflux from striatal slices during development and after nigrostriatal bundle damage. *J Neurosci* **7**, 1648-1654 (1987).
8. P. Gonzalez-Rodriguez *et al.*, Disruption of mitochondrial complex I induces progressive parkinsonism. *Nature* **599**, 650-656 (2021).
9. M. W. Bishop *et al.*, Hyperexcitable substantia nigra dopamine neurons in PINK1- and HtrA2/Omi-deficient mice. *J Neurophysiol* **104**, 3009-3020 (2010).
10. J. Schiemann *et al.*, K-ATP channels in dopamine substantia nigra neurons control bursting and novelty-induced exploration. *Nat Neurosci* **15**, 1272-1280 (2012).
11. H. Morikawa, C. A. Paladini, Dynamic regulation of midbrain dopamine neuron activity: intrinsic, synaptic, and plasticity mechanisms. *Neuroscience* **198**, 95-111 (2011).
12. H. Bergman, T. Wichmann, B. Karmon, M. R. DeLong, The primate subthalamic nucleus. II. Neuronal activity in the MPTP model of parkinsonism. *J Neurophysiol* **72**, 507-520 (1994).
13. A. Dagra *et al.*, alpha-Synuclein-induced dysregulation of neuronal activity contributes to murine dopamine neuron vulnerability. *NPJ Parkinsons Dis* **7**, 76 (2021).
14. M. Regoni *et al.*, Pharmacological antagonism of kainate receptor rescues dysfunction and loss of dopamine neurons in a mouse model of human parkin-induced toxicity. *Cell Death Dis* **11**, 963 (2020).
15. S. Janezic *et al.*, Deficits in dopaminergic transmission precede neuron loss and dysfunction in a new Parkinson model. *Proc Natl Acad Sci U S A* **110**, E4016-4025 (2013).
16. P. D. Dodson *et al.*, Representation of spontaneous movement by dopaminergic neurons is cell-type selective and disrupted in parkinsonism. *Proc Natl Acad Sci U S A* **113**, E2180-2188 (2016).

17. M. Subramaniam *et al.*, Mutant alpha-synuclein enhances firing frequencies in dopamine substantia nigra neurons by oxidative impairment of A-type potassium channels. *J Neurosci* **34**, 13586-13599 (2014).
18. J. S. Chou *et al.*, (G2019S) LRRK2 causes early-phase dysfunction of SNpc dopaminergic neurons and impairment of corticostriatal long-term depression in the PD transgenic mouse. *Neurobiol Dis* **68**, 190-199 (2014).
19. H. Braak, K. Del Tredici, Poor and protracted myelination as a contributory factor to neurodegenerative disorders. *Neurobiol Aging* **25**, 19-23 (2004).
20. P. Tagliaferro, R. E. Burke, Retrograde Axonal Degeneration in Parkinson Disease. *J Parkinsons Dis* **6**, 1-15 (2016).
21. D. Haddad, K. Nakamura, Understanding the susceptibility of dopamine neurons to mitochondrial stressors in Parkinson's disease. *FEBS Lett* **589**, 3702-3713 (2015).
22. R. Betarbet *et al.*, Chronic systemic pesticide exposure reproduces features of Parkinson's disease. *Nat Neurosci* **3**, 1301-1306 (2000).
23. Z. Doric, K. Nakamura, Mice with disrupted mitochondria used to model Parkinson's disease. *Nature* **599**, 558-560 (2021).
24. A. Berthet *et al.*, Loss of mitochondrial fission depletes axonal mitochondria in midbrain dopamine neurons. *J Neurosci* **34**, 14304-14317 (2014).
25. H. Li *et al.*, Longitudinal tracking of neuronal mitochondria delineates PINK1/Parkin-dependent mechanisms of mitochondrial recycling and degradation. *Sci Adv* **7**, (2021).
26. C. Pacelli *et al.*, Elevated Mitochondrial Bioenergetics and Axonal Arborization Size Are Key Contributors to the Vulnerability of Dopamine Neurons. *Curr Biol* **25**, 2349-2360 (2015).
27. B. Piallat, A. Benazzouz, A. L. Benabid, Subthalamic nucleus lesion in rats prevents dopaminergic nigral neuron degeneration after striatal 6-OHDA injection: behavioural and immunohistochemical studies. *Eur J Neurosci* **8**, 1408-1414 (1996).
28. H. Bergman, T. Wichmann, M. R. DeLong, Reversal of experimental parkinsonism by lesions of the subthalamic nucleus. *Science* **249**, 1436-1438 (1990).
29. K. A. B. Zaghloul, J. A.; Weidemann, C. T.; McGill, K.; Jaggi, J. L.; Baltuch, G. H.; Kahana, M. J., Human Substantia Nigra Neurons Encode Unexpected Financial Rewards. *Science* **323**, 1496-1499 (2009).
30. J. A. da Silva, F. Tecuapetla, V. Paixao, R. M. Costa, Dopamine neuron activity before action initiation gates and invigorates future movements. *Nature* **554**, 244-248 (2018).
31. X. Jin, R. M. Costa, Start/stop signals emerge in nigrostriatal circuits during sequence learning. *Nature* **466**, 457-462 (2010).
32. A. V. Kravitz *et al.*, Regulation of parkinsonian motor behaviours by optogenetic control of basal ganglia circuitry. *Nature* **466**, 622-626 (2010).
33. S. Wang, Y. Tan, J. E. Zhang, M. Luo, Pharmacogenetic activation of midbrain dopaminergic neurons induces hyperactivity. *Neurosci Bull* **29**, 517-524 (2013).
34. J. H. Kordower *et al.*, Disease duration and the integrity of the nigrostriatal system in Parkinson's disease. *Brain* **136**, 2419-2431 (2013).
35. B. L. Roth, DREADDs for Neuroscientists. *Neuron* **89**, 683-694 (2016).
36. R. Donato, Intracellular and extracellular roles of S100 proteins. *Microsc Res Tech* **60**, 540-551 (2003).

37. F. Lang, N. Strutz-Seebohm, G. Seebohm, U. E. Lang, Significance of SGK1 in the regulation of neuronal function. *J Physiol* **588**, 3349-3354 (2010).
38. A. Filipek, W. Lesniak, S100A6 and Its Brain Ligands in Neurodegenerative Disorders. *Int J Mol Sci* **21**, (2020).
39. S. Iwata, M. Nomoto, H. Morioka, A. Miyata, Gene expression profiling in the midbrain of striatal 6-hydroxydopamine-injected mice. *Synapse* **51**, 279-286 (2004).
40. C. C. Stichel *et al.*, sgk1, a member of an RNA cluster associated with cell death in a model of Parkinson's disease. *Eur J Neurosci* **21**, 301-316 (2005).
41. A. R. Means, M. F. VanBerkum, I. Bagchi, K. P. Lu, C. D. Rasmussen, Regulatory functions of calmodulin. *Pharmacol Ther* **50**, 255-270 (1991).
42. Y. J. Hsu, J. G. Hoenderop, R. J. Bindels, TRP channels in kidney disease. *Biochim Biophys Acta* **1772**, 928-936 (2007).
43. J. Xu, Z. P. Pang, O. H. Shin, T. C. Sudhof, Synaptotagmin-1 functions as a Ca2+ sensor for spontaneous release. *Nat Neurosci* **12**, 759-766 (2009).
44. A. Kadkova, J. Radecke, J. B. Sorensen, The SNAP-25 Protein Family. *Neuroscience* **420**, 50-71 (2019).
45. L. P. Jackson *et al.*, A large-scale conformational change couples membrane recruitment to cargo binding in the AP2 clathrin adaptor complex. *Cell* **141**, 1220-1229 (2010).
46. P. W. Ho *et al.*, In vivo overexpression of synaptogyrin-3 promotes striatal synaptic dopamine uptake in LRRK2(R1441G) mutant mouse model of Parkinson's disease. *Brain Behav* **13**, e2886 (2023).
47. J. T. Bendor, T. P. Logan, R. H. Edwards, The function of alpha-synuclein. *Neuron* **79**, 1044-1066 (2013).
48. E. Carpene, G. Andreani, G. Isani, Metallothionein functions and structural characteristics. *J Trace Elem Med Biol* **21 Suppl 1**, 35-39 (2007).
49. R. F. Fernandez, J. M. Ellis, Acyl-CoA synthetases as regulators of brain phospholipid acyl-chain diversity. *Prostaglandins Leukot Essent Fatty Acids* **161**, 102175 (2020).
50. J. S. Dittman, Unc13: a multifunctional synaptic marvel. *Curr Opin Neurobiol* **57**, 17-25 (2019).
51. F. P. Diekstra *et al.*, C9orf72 and UNC13A are shared risk loci for amyotrophic lateral sclerosis and frontotemporal dementia: a genome-wide meta-analysis. *Ann Neurol* **76**, 120-133 (2014).
52. J. P. Quinn, S. E. Kandigian, B. A. Trombetta, S. E. Arnold, B. C. Carlyle, VGF as a biomarker and therapeutic target in neurodegenerative and psychiatric diseases. *Brain Commun* **3**, fcab261 (2021).
53. A. Eban-Rothschild, G. Rothschild, W. J. Giardino, J. R. Jones, L. de Lecea, VTA dopaminergic neurons regulate ethologically relevant sleep-wake behaviors. *Nat Neurosci* **19**, 1356-1366 (2016).
54. M. Helwig *et al.*, Neuronal hyperactivity-induced oxidant stress promotes in vivo alpha-synuclein brain spreading. *Sci Adv* **8**, eabn0356 (2022).
55. D. G. Harden, A. A. Grace, Activation of dopamine cell firing by repeated L-DOPA administration to dopamine-depleted rats: its potential role in mediating the therapeutic response to L-DOPA treatment. *J Neurosci* **15**, 6157-6166 (1995).

56. B. Liss, R. Bruns, J. Roeper, Alternative sulfonylurea receptor expression defines metabolic sensitivity of K-ATP channels in dopaminergic midbrain neurons. *EMBO J* **18**, 833-846 (1999).
57. G. Bilbao *et al.*, Electrophysiological characterization of substantia nigra dopaminergic neurons in partially lesioned rats: effects of subthalamotomy and levodopa treatment. *Brain Res* **1084**, 175-184 (2006).
58. B. Liss *et al.*, K-ATP channels promote the differential degeneration of dopaminergic midbrain neurons. *Nat Neurosci* **8**, 1742-1751 (2005).
59. A. G. Yee *et al.*, Effects of the Parkinsonian toxin MPP+ on electrophysiological properties of nigral dopaminergic neurons. *Neurotoxicology* **45**, 1-11 (2014).
60. M. Y. Jing *et al.*, Re-examining the role of ventral tegmental area dopaminergic neurons in motor activity and reinforcement by chemogenetic and optogenetic manipulation in mice. *Metab Brain Dis* **34**, 1421-1430 (2019).
61. N. E. Taylor *et al.*, Optogenetic activation of dopamine neurons in the ventral tegmental area induces reanimation from general anesthesia. *Proc Natl Acad Sci U S A* **113**, 12826-12831 (2016).
62. S. Imai, N. Okayama, M. Shimizu, M. Itoh, Increased intracellular calcium activates serum and glucocorticoid-inducible kinase 1 (SGK1) through a calmodulin-calcium calmodulin dependent kinase kinase pathway in Chinese hamster ovary cells. *Life Sci* **72**, 2199-2209 (2003).
63. C. S. Chan *et al.*, 'Rejuvenation' protects neurons in mouse models of Parkinson's disease. *Nature* **447**, 1081-1086 (2007).
64. D. J. Surmeier, P. T. Schumacker, Calcium, bioenergetics, and neuronal vulnerability in Parkinson's disease. *J Biol Chem* **288**, 10736-10741 (2013).
65. A. Abdanipour *et al.*, Neuroprotective effects of selegiline on rat neural stem cells treated with hydrogen peroxide. *Biomed Rep* **8**, 41-46 (2018).
66. M. Elkenani *et al.*, Heat shock protein A4 ablation leads to skeletal muscle myopathy associated with dysregulated autophagy and induced apoptosis. *J Transl Med* **20**, 229 (2022).
67. Y. Yang *et al.*, SIRT1 attenuates neuroinflammation by deacetylating HSPA4 in a mouse model of Parkinson's disease. *Biochim Biophys Acta Mol Basis Dis* **1868**, 166365 (2022).
68. M. Quik, Smoking, nicotine and Parkinson's disease. *Trends Neurosci* **27**, 561-568 (2004).
69. J. B. Nourse, Jr. *et al.*, Conserved nicotine-activated neuroprotective pathways involve mitochondrial stress. *iScience* **24**, 102140 (2021).
70. C. Xiao *et al.*, Chronic nicotine selectively enhances alpha4beta2* nicotinic acetylcholine receptors in the nigrostriatal dopamine pathway. *J Neurosci* **29**, 12428-12439 (2009).
71. M. L. Hacker *et al.*, Deep brain stimulation in early-stage Parkinson disease: Five-year outcomes. *Neurology* **95**, e393-e401 (2020).
72. C. M. Backman *et al.*, Characterization of a mouse strain expressing Cre recombinase from the 3' untranslated region of the dopamine transporter locus. *Genesis* **44**, 383-390 (2006).
73. Y. Fu *et al.*, A cytoarchitectonic and chemoarchitectonic analysis of the dopamine cell groups in the substantia nigra, ventral tegmental area, and retrorubral field in the mouse. *Brain Struct Funct* **217**, 591-612 (2012).

74. Y. J. Sei, M. M. Chaumeil, K. Nakamura, Protocol to combine brain sections from multiple mice into a single block for spatial transcriptomic analyses. *STAR Protoc* **4**, 102617 (2023).
75. E. Y. Chen *et al.*, Enrichr: interactive and collaborative HTML5 gene list enrichment analysis tool. *BMC Bioinformatics* **14**, 128 (2013).
76. M. V. Kuleshov *et al.*, Enrichr: a comprehensive gene set enrichment analysis web server 2016 update. *Nucleic Acids Res* **44**, W90-97 (2016).
77. Z. Xie *et al.*, Gene Set Knowledge Discovery with Enrichr. *Curr Protoc* **1**, e90 (2021).
78. E. Gibbels, [Hitler's Parkinson syndrome. A posthumous motility analysis of film records of the German Weekly News 1940-1945]. *Nervenarzt* **59**, 521-528 (1988).
79. H. Braak *et al.*, Staging of brain pathology related to sporadic Parkinson's disease. *Neurobiol Aging* **24**, 197-211 (2003).
80. G. M. Halliday, K. Del Tredici, H. Braak, Critical appraisal of brain pathology staging related to presymptomatic and symptomatic cases of sporadic Parkinson's disease. *J Neural Transm Suppl*, 99-103 (2006).
81. L. van Hijfte *et al.*, Alternative normalization and analysis pipeline to address systematic bias in NanoString GeoMx Digital Spatial Profiling data. *iScience* **26**, 105760 (2023).
82. I. Korsunsky *et al.*, Fast, sensitive and accurate integration of single-cell data with Harmony. *Nat Methods* **16**, 1289-1296 (2019).
83. C. W. Law, Y. Chen, W. Shi, G. K. Smyth, voom: Precision weights unlock linear model analysis tools for RNA-seq read counts. *Genome Biol* **15**, R29 (2014).

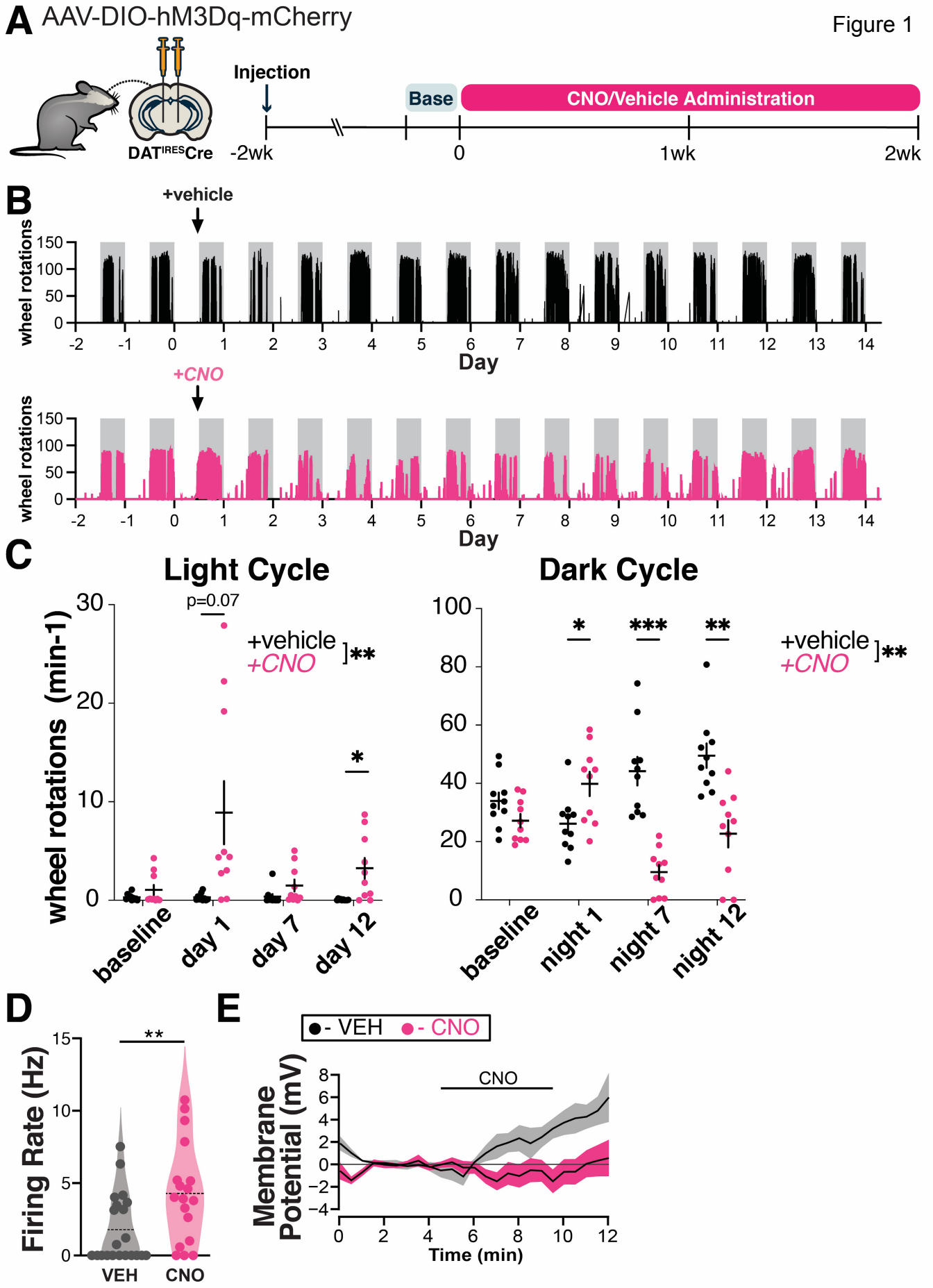
Figure 1
A
AAV-DIO-hM3Dq-mCherry
DAT IRES Cre
Injection
Base
CNO/Vehicle Administration
-2wk
0
1wk
2wk
B
+vehicle
wheel rotations
Day
+CNO
C
Light Cycle
Dark Cycle
wheel rotations (min-1)
p=0.07
+vehicle
+CNO
baseline
day 1
day 7
day 12
night 1
night 7
night 12
D
Firing Rate (Hz)
VEH
CNO
E
- VEH
- CNO
CNO
Membrane Potential (mV)
Time (min)

2 weeks

4 weeks

A

anti-TH

+Veh

+CNO

CPu

NAc

Core

Shell

OT

+vehicle +CNO

optical density (normalized)

1.5 1.0 0.5 0.0

** n.s. n.s. n.s.

*** * n.s.

CPu NAc-C NAc-Sh OT

B

anti-mCherry

CPu

core

shell

NAc

OT

fluorescence density (normalized)

*** ** ** n.s.

*** n.s. n.s.

CPu NAc-C NAc-Sh OT

C

anti-TH

VTA

SN

+Vehicle

+CNO

number of TH+ Cells

10000 8000 6000 4000 2000 0

n.s. n.s.

SN VTA

D

anti-TH

+Vehicle Gq-

+CNO Gq-

CPu

core

shell

NAc

OT

optical density (normalized)

1.5 1.0 0.5 0.0

n.s. n.s. n.s. n.s.

CPu NAcC NAcSh OT

E

anti-TH

+Vehicle

+CNO

CPu

Core

NAc

Shell

OT

+vehicle +CNO

optical density (normalized)

1.5 1.0 0.5 0.0

** n.s. n.s. n.s.

CPu NAc-C NAc-Sh OT

F

anti-mCherry

CPu

Core

NAc

Shell

OT

fluorescence density (normalized)

1.5 1.0 0.5 0.0

* n.s. n.s. n.s.

CPu NAc-C NAc-Sh OT

G

anti-TH

+Vehicle

+CNO

VTA

SN

number of TH+ Cells

10000 8000 6000 4000 2000 0

+vehicle +CNO]*

p=0.1

SN VTA

H

anti-mCherry

+Vehicle

+CNO

number of mCherry+ Cells

10000 8000 6000 4000 2000 0

+vehicle +CNO]**

p=0.1 *

SN VTA

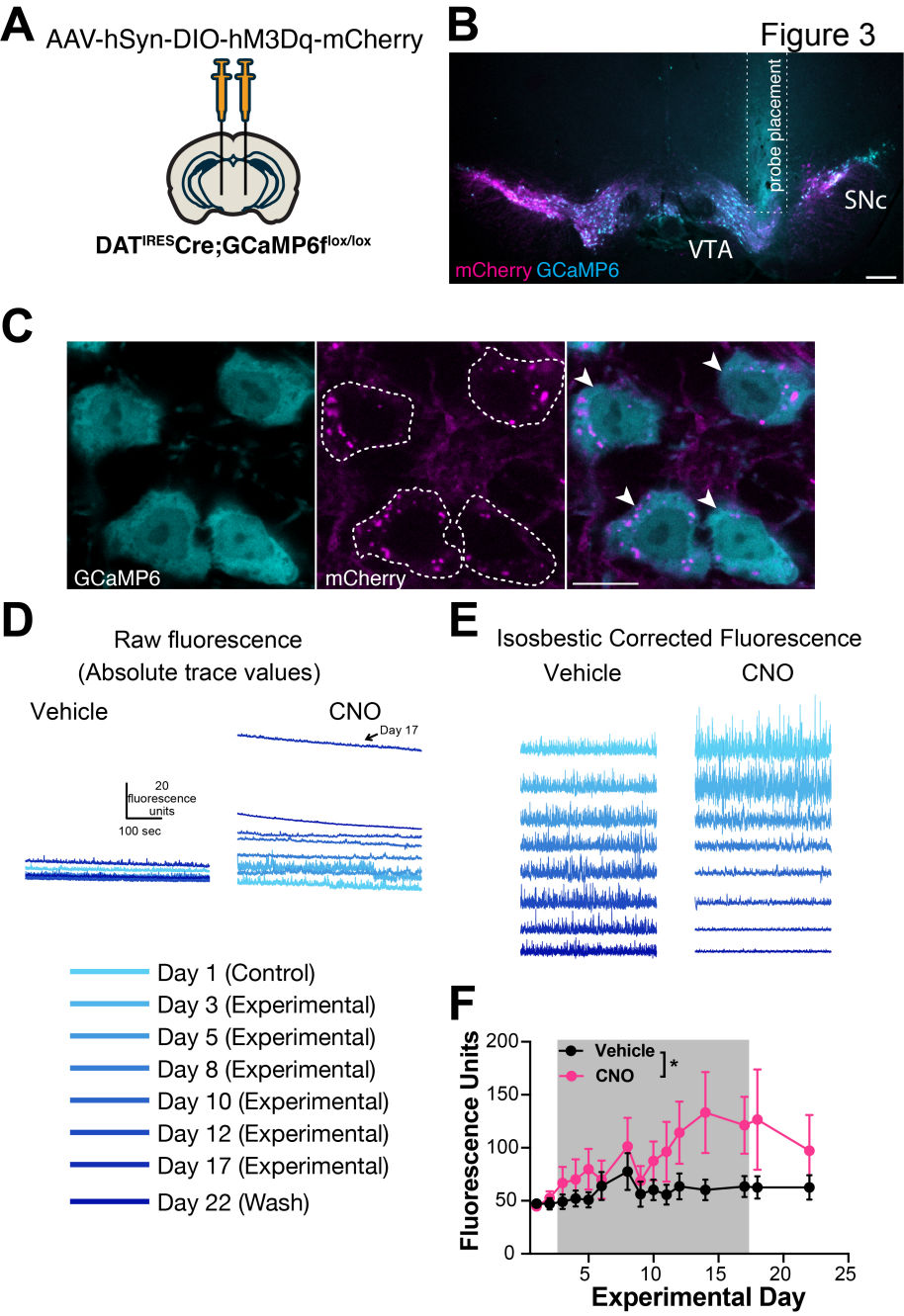
A
AAV-hSyn-DIO-hM3Dq-mCherry
DATIRESCre;GCaMP6flox/lox
B
Figure 3
probe placement
SNc
VTA
mCherry GCaMP6
C
GCaMP6
mCherry
D
Raw fluorescence
(Absolute trace values)
Vehicle
CNO
Day 17
20
fluorescence
units
100 sec
Day 1 (Control)
Day 3 (Experimental)
Day 5 (Experimental)
Day 8 (Experimental)
Day 10 (Experimental)
Day 12 (Experimental)
Day 17 (Experimental)
Day 22 (Wash)
E
Isosbestic Corrected Fluorescence
Vehicle
CNO
F
Vehicle
CNO
*
Fluorescence Units
Experimental Day
0
50
100
150
200
5
10
15
20
25

Figure 4

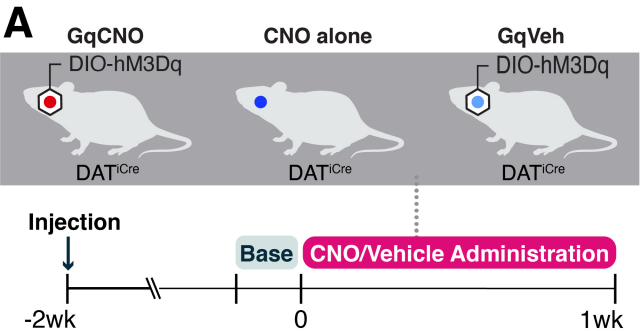
A
GqCNO
CNO alone
GqVeh
DIO-hM3Dq
DIO-hM3Dq
DATiCre
DATiCre
DATiCre
Injection
Base
CNO/Vehicle Administration
-2wk
0
1wk

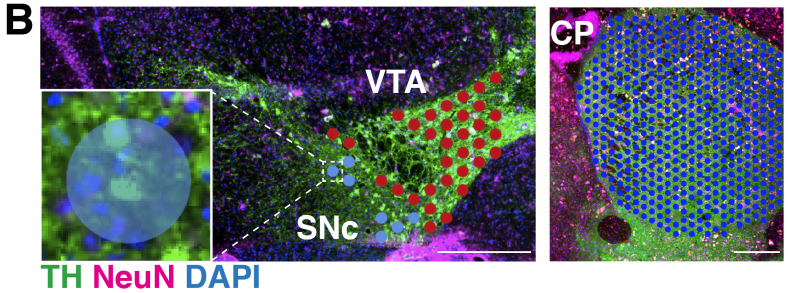
B
VTA
SNc
CP
TH NeuN DAPI

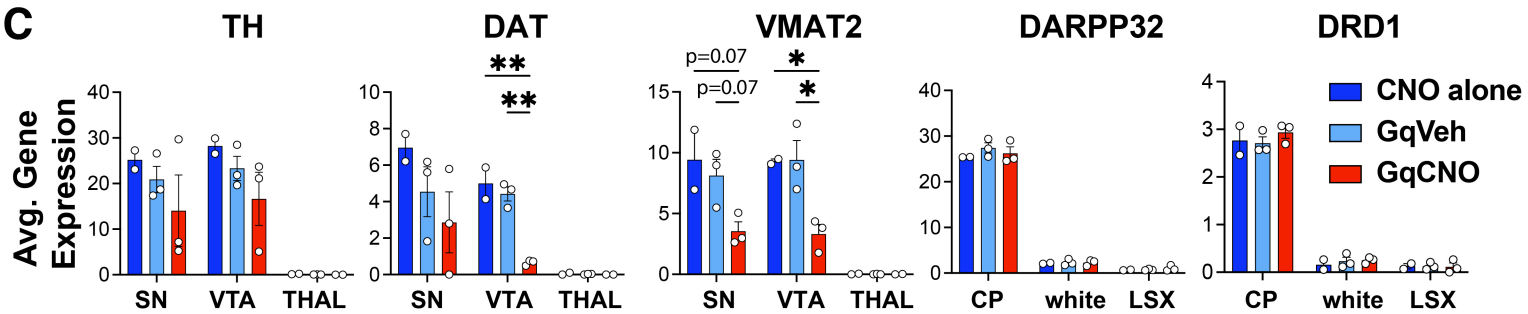
C
TH
DAT
VMAT2
DARPP32
DRD1
Avg. Gene Expression
p=0.07
p=0.07
CNO alone
GqVeh
GqCNO
SN
VTA
THAL
CP
white
LSX

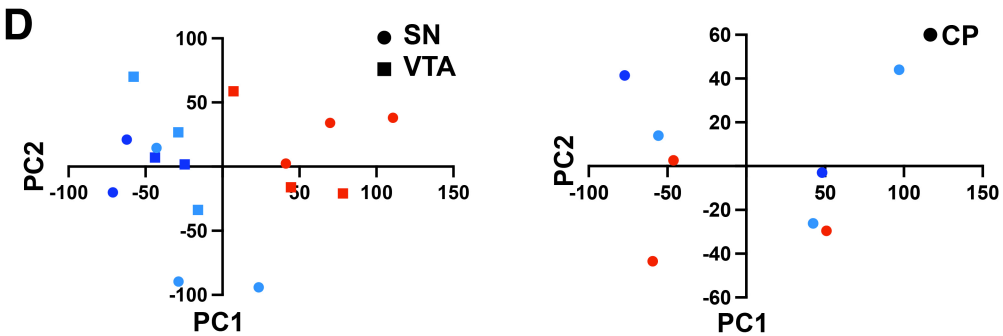
D
SN
VTA
CP
PC1
PC2

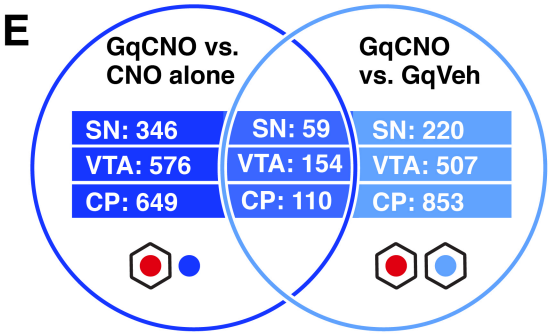
E
GqCNO vs. CNO alone
GqCNO vs. GqVeh
SN: 346
VTA: 576
CP: 649
SN: 59
VTA: 154
CP: 110
SN: 220
VTA: 507
CP: 853

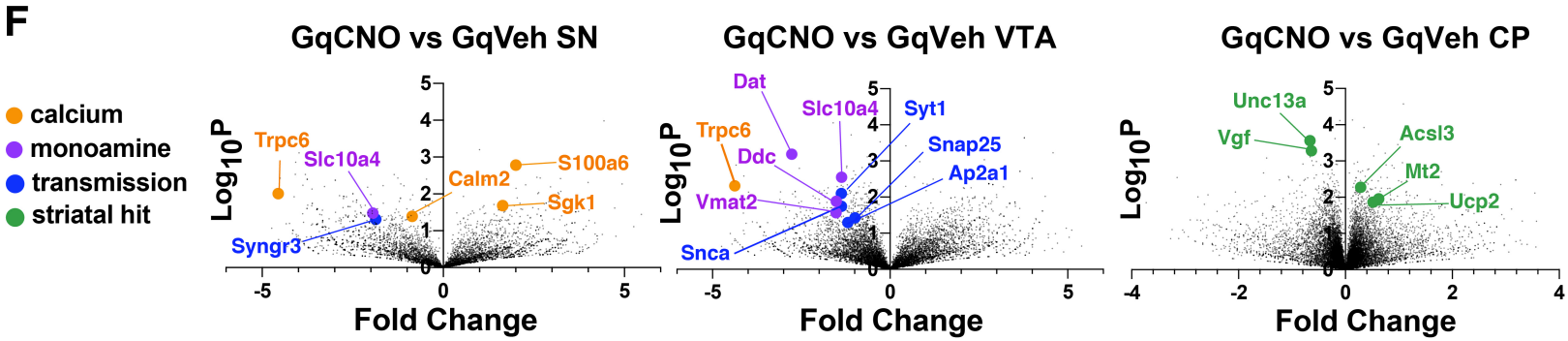
F
GqCNO vs GqVeh SN
GqCNO vs GqVeh VTA
GqCNO vs GqVeh CP
calcium
monoamine
transmission
striatal hit
Log10P
Fold Change
Trpc6
Slc10a4
Syngr3
Calm2
S100a6
Sgk1
Dat
Slc10a4
Syt1
Trpc6
Ddc
Snap25
Ap2a1
Vmat2
Snca
Unc13a
Vgf
Acsl3
Mt2
Ucp2